

Research Paper

## Effect of Laser Parameters on Geometry of Cladded Stellite 6 on 35CrMo Steel Substrate and its Characterization

**Bahman Mansouri<sup>1</sup>, Mahdi Rafiei<sup>1\*</sup>, Iman Ebrahimzadeh<sup>1</sup>, Farid Naeimi<sup>1</sup>, Masoud Barekat<sup>2</sup>**

*1. Advanced Materials Research Center, Department of Materials Engineering, Najafabad Branch, Islamic Azad University, Najafabad, Iran.*

*2. Faculty of Materials and Manufacturing Engineering, Malek Ashtar University of Technology, Tehran. Iran.*

---

### ARTICLE INFO

---

#### Article history:

Received 26 April 2024  
Accepted 14 October 2024  
Available online 1 May 2023

---

#### Keywords:

*Laser cladding  
Microstructure  
Stellite 6  
35CrMo alloy steel  
Overlapping  
Microhardness*

---

### ABSTRACT

In this research, laser cladding of Stellite 6 on the 35CrMo substrate was done. Various parameters of the laser cladding process were studied and after optimization of the parameters, microstructure and microhardness were evaluated. Characterization of the cladded layer was done by scanning electron microscope, X-ray diffraction, and Vickers microhardness. The results show that the clad track height was dependent on the parameters of the powder feeding rate and the laser scanning speed, and the laser power had the minimal effect. Similarly, the clad track width was controlled by the laser power and laser scanning speed. The clad track dilution was proportional to the laser power and had the greatest impact compared to other parameters. The wetting angle was controlled by three parameters: laser power, laser scanning speed, and powder feeding rate. Laser power of 550 W, powder feeding rate of 0.6 g/s, and laser scanning speed of 10 mm/s were chosen as the optimal parameters. The results showed a good metallurgical bonding between the cladding and the substrate. The microstructure of the single clad track was dense and crack- and pore-free, and due to the thermal and concentration gradient changes during solidification, it consisted of three different areas, including planar, columnar dendritic, and equiaxed dendritic microstructures. A significant improvement in the microhardness of Stellite 6 cladding was observed as compared with the substrate. By increasing the overlapping ratio from 30 to 60%, the dilution rate decreased from 31 to 7%. As a result, the microhardness reached 361 HV in the overlapping ratio of 30% and further to 452 HV in the overlapping ratio of 60%. The overlapping ratio of 60% between adjacent passes created the best results.

---

**Citation:** Mansouri, B.; Rafiei, M.; Ebrahimzadeh, I.; Naeimi, F.; Barekat, M. (2023). Effect of Laser Parameters on Geometry of Cladded Stellite 6 on 35CrMo Steel Substrate and its Characterization, Journal of Advanced Materials and Processing, 11 (2), 41-53. Doi: 10.71670/jmatpro.2024.1115395

#### Copyrights:

Copyright for this article is retained by the author (s), with publication rights granted to Journal of Advanced Materials and Processing. This is an open – access article distributed under the terms of the Creative Commons Attribution License (<http://creativecommons.org/licenses/by/4.0>), which permits unrestricted use, distribution and reproduction in any medium, provided the original work is properly cited.



---

\* **Corresponding Author:**

E-Mail: m.rafiei@pmt.iau.ac.ir

## 1. Introduction

35CrMo alloy steel, owing to its properties such as good hardness, suitable fatigue strength, high strength, and good machining ability [1], is widely used in the fabrication of hot roll rollers, steam turbine engines, and petroleum machines [2, 3]. It is also used as a common material for gears, bearings, and transmission shafts due to its excellent mechanical properties [4-8]. For this type of application, plastic deformation is a common damage phenomenon because of stress concentration effects [9]. Also, the poor wear and corrosion properties of this material are two main reasons for limiting its application [10]. Creating new layers by laser cladding method to repair the local defects of machines, the production of wear and corrosion-resistant coatings, repair worn-out parts by adding materials, or the production of new structures for rapid prototyping [11,12] is used in the military, aerospace, rail transportation, etc. [13]. The advantages of laser cladding compared to other common methods such as tungsten arc welding, thermal and flame spraying of thin coating deposits, are minimal dilution, minimal distortion, a low heat-affected zone, low holes and cracks, and controllable thickness on the desired surface [12, 14]. Basically, there are two possible methods to use cladding material. The first mode is the use of pre-placed material on the substrate. This process is usually time-consuming, requires a higher power beam for complete melting and mixing with the substrate, and is applied on limited shapes of the substrate [12, 15, 16]. The second one is laser cladding with injected powder. In this method, the powder is injected by gas carrier, and it is blown under the laser beam on the substrate and creates a molten pool, and as a result, a single clad track is produced. The powder injection can be either off-axis or coaxial by ring nozzle or multiple discrete nozzles [12, 15, 16]. The powder injection process results in complete dense cladding. The overlap influences the final thickness of the cladding, the dilution, and thus the final functional properties of the cladding. If the overlap is insufficient, the dilution is too high, and excessive mixing of cladding material with substrate occurs. This may lead to a decrease in the functional properties of the cladding, such as wear and corrosion resistance [17, 18].

Co-based alloys are used due to their high strength, resistance to oxidation and corrosion, resistance to fatigue and creep [12], and resistance to solidification cracks in the melting region [19]. Stellites are a type of Co-based superalloy, and Stellite 6 is one of the most common alloys for a wide range of surface hardening applications [20]. The strength in these alloys is achieved by two mechanisms, including the

strengthening of the solid solution with the presence of elements such as Cr, W, Ni, and Mo and the formation of carbides (commonly due to the addition of Cr) [12, 19, 21-22]. In terms of microstructure, the wear resistance of Stellite 6 alloy is attributed to the high amount of Cr<sub>7</sub>C<sub>3</sub> carbides in the interdendritic regions [20]. According to the mentioned properties, Co-based alloys are widely used as cladding in the chemical, oil, and gas industries, including seat and gate valves, steam turbine blades, bearings, shafts, and many industrial components [23-25]. Valsecchi et al. [26] investigated the laser cladding of Co base powder on martensitic stainless steel substrate. The metallurgical characteristics of the clad layer, the substrate, and also the clad height were investigated. Although the powder feeding rate was the same in samples, the clad height was lower in the case where less laser energy was used. The clad zone showed the dendritic microstructure. With the increase of laser energy, the grains became coarser, which can be attributed to the lower solidification rate. All samples had a much higher microhardness than the substrate. Chang et al. [27] investigated the laser cladding of Stellite 6 on the Cr-Mo-V steel substrate with the aim of improving wear resistance as compared with the plasma spraying. In the laser cladding sample, the microstructure included a hypoeutectic structure with primary gamma dendrites, the Co-base solid solution, and interdendritic eutectics. In the plasma spraying sample, a layered eutectic structure was created in the interdendritic regions. In general, the laser cladding, which obtained the fine-grained structure, showed an increase in hardness, toughness, and wear resistance compared to the plasma spraying method. Lin et al. [28] investigated the structure caused by the deposition of a thin layer of Stellite 6 on a mild carbon steel substrate using the laser cladding method. The cladding layer showed a crack-free structure with very good metallurgical bonding to the substrate. Also, the hardness of the sample after laser cladding increased as compared to the substrate. Sun et al. [29] investigated the laser cladding of Stellite 6 alloy on an AISI 420 stainless steel substrate. The effect of pulse energy, pulse frequency, and powder feeding rate on clad height, dilution, and heat-affected zone (HAZ) was investigated. The results showed that the clad height and the depth of the penetration zone to the substrate increase with the laser energy, pulse frequency, and overlapping percentage. The coatings were crack-free, had a low penetration depth to the substrate, and had a smaller HAZ. Oliveira et al. [30] investigated one, two, and five layers of laser cladding of Stellite 6 on an AISI 304 stainless steel substrate. The effect of multilayer structure on the microstructure and residual stresses

was studied in single-layer samples. For this reason, a decrease in residual stress was observed, which is caused by a high rate of plastic deformation. In multilayer samples, because the rate of deformation was lower, an increase in thermal gradient and residual stresses was observed. The cross-sectional microstructure of the samples in two regions of the cladding surface and near the interface showed that with the increase in number of layers, coarse interdendritic regions were created near the interface. Xu et al. [31] investigated laser cladding of Stellite 6/WC with different amounts of WC particles on a mild carbon steel substrate. With the increase of WC deposits in different amounts (range 0-90%), hardness and wear resistance increased. By increasing the amount of WC to more than 90%, due to a significant increase in penetration, a decrease in wear resistance was observed. The purpose of this research is to increase the hardness of 35CrMo alloy steel for use in hot roll rollers, petroleum machines, steam turbine engines, bearings, and transmission shafts. Therefore, investigating the behavior of Stellite 6 cladding on 35CrMo alloy steel substrates can provide appropriate practical information to develop the industrial application of 35CrMo alloys. In the present research, for the first time, the characteristics of laser-cladded

Stellite 6 on the surface of 35CrMo alloy steel were investigated. Also, optimizing the Stellite 6 cladding using different parameters of laser cladding, the effect of overlapping ratio, microstructure, and mechanical properties of the cladding were investigated.

## 2. Materials and methods

In this research, 35CrMo alloy steel disks with the diameter of 70 mm and the thickness of 6 mm were used as the substrate material. The chemical composition of this steel is listed in Table 1. The substrate was cleaned with sandpaper to remove surface oxides or contaminants. After that, the sample was first degreased, then immersed in acetone with the ultrasonic method, and then washed with distilled water and alcohol and dried in a cold airstream. Co-base alloy powder of Stellite 6 (PAC companies, USA) according to the XRD pattern presented in Fig. 1 was used for the laser cladding process. The chemical composition of Stellite 6 powder is listed in Table 2. Fig. 2 shows the distribution and particle size of Stellite 6 powder with spherical morphology. According to Fig. 2, the average particle size of Stellite 6 powder is 30-100  $\mu\text{m}$ .

**Table 1.** The chemical composition of the 35CrMo alloy steel (wt.%)

Fe	C	Si	Mn	Mo	Cr
Bal.	0.32-0.40	0.17-0.37	0.40-0.70	0.15-0.25	0.80- 1.10

**Table 2.** The chemical composition of the Co base alloy powder of Stellite 6 (wt.%)

Co	C	Mo	Ni	Fe	Mn	Cr	Si
Bal.	7.43	0.50	3.34	2.03	1.37	30.76	2.17

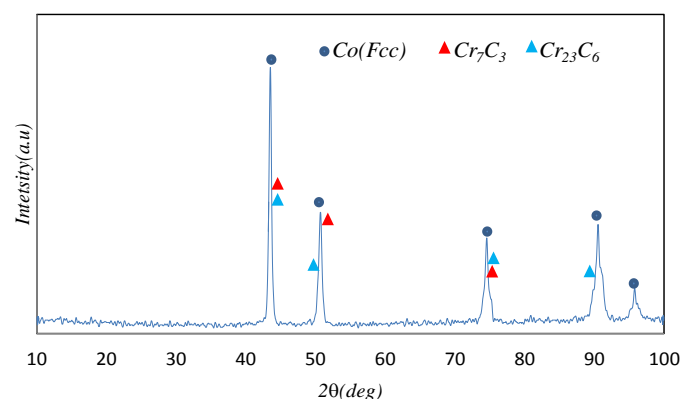


**Fig.1.** XRD pattern of Stellite 6 powder

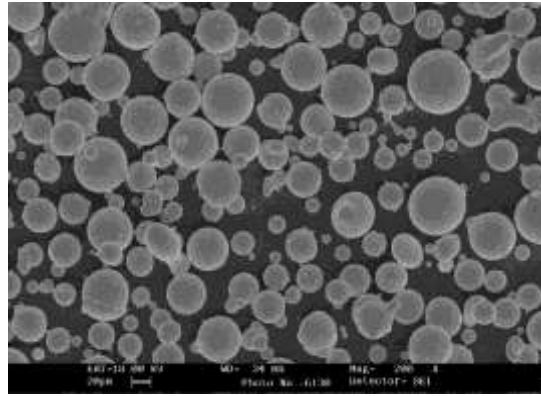


**Fig. 2.** SEM micrograph of Stellite 6 powder

The powders were dried in an oven at a temperature of 120 °C for 1 h before being coaxially injected into the molten pool. Laser cladding was done using a 1 kW pulsed fiber laser equipped with a 5-axis computer numerical controlled (CNC) machine under an Ar environment. In all experiments, the laser beam was focused exactly on the substrate surface with a spot size of 1 mm. A schematic of the

laser cladding process is shown in Fig. 3. The primary variables of single-pass laser cladding are shown in Table 3. In order to achieve an appropriate cladding, different parameters of the laser were investigated by the full factorial method. Laser cladding parameters were selected experimentally after some tests on the real samples and characterization of them.

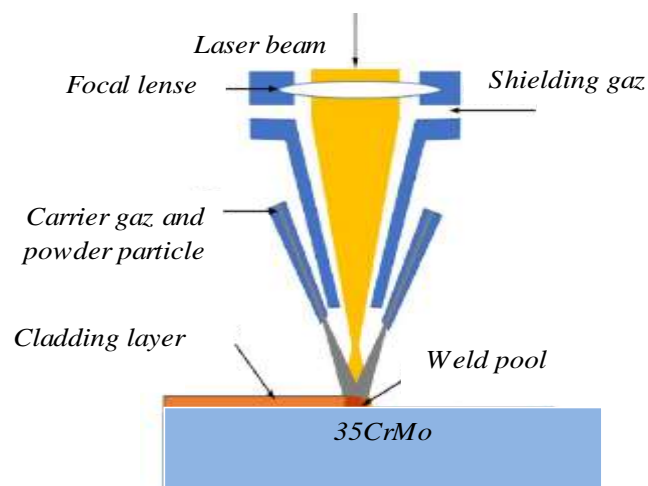


**Fig. 3.** Schematic of the laser cladding process

**Table 3.** Laser parameters used in this research

Processing parameter	Value
Laser power (W)	250-850
laser scanning speed (mm/s)	6,8,10
Powder feeding rate (gr/s)	0.2, 0.4,0.6
Shielding gas flow rate (l/min)	15
Powder carried gas flow rate (l/min)	20

After identifying the optimal parameters of power laser (P), laser scanning speed (S), and powder feeding rate (F), the cladding process was carried out with different overlapping ratios (OR) of 30, 40, 50, and 60%. To create cladding, after each pass, the laser beam was turned off, and the nozzle quickly moved to the new starting point, and the next pass was applied. After laser cladding in single pass mode

with different ORs, metallographic specimens were cut from the cross section, sanded with 60-3000 grit sandpaper, polished with 0.3  $\mu\text{m}$  alumina powder, and then were chemically etched in  $\text{HCl}:\text{HNO}_3=3:1$  solution. The microstructure of cladding and powder and cladding geometry were observed using a scanning electron microscope (SEM) in a Philips XL30. Using the image analysis software, the

geometric characteristics of the cladding (clad width (W), clad height (H), clad penetration depth (b) in substrate, and the wetting angle) were evaluated to achieve the optimal parameters. The phase analysis of the powders and claddings was done by X-ray diffraction (XRD) in a Philips X'PERT MPD diffractometer using filtered Cu- $\alpha$  radiation ( $\lambda = 0.1542$  nm). A microhardness test was performed using a Vickers microhardness tester (Micromet model, Buehler) at a load of 300 g and a dwell time of 15 s according to the ASTM E384-99 standard. The average values of three measurements were reported as the microhardness number of each sample.

### 3. Results and discussion

#### 3.1. Optimization of Stellite 6 cladding using different laser cladding parameters

Fig. 4 shows cross-sectional SEM micrographs of single clad tracks of Stellite 6 for each laser power, laser scanning speed, and powder feeding rate. As can be seen in Fig. 4, in low values of laser power, the substrate is less melted, which leads to the detaching of the clad track. According to the results of Fig. 4, the clad height changes from 118 to 1993  $\mu\text{m}$ . Also, the laser track height increases with increasing the amount of powder feeding rate as well as reducing the laser scanning speed. According to the results, by keeping all process parameters constant, increasing or reducing the laser power had a lower effect on the clad height. By increasing the powder feeding rate and reducing the laser scanning speed, interaction between powder and laser energy increases, and therefore, more amounts of powder reach molten temperature, leading to more height of the clad track. This issue is in agreement with the research results of Toyserkani et al. [32] and Barekat et al. [33]. According to Fig. 4, the value of clad tracks width changes from 1.39 to 2.567 mm. According to the results, by increasing the laser power and decreasing the laser scanning speed, the clad track width increased. Also, the laser power effect was greater than the laser scanning speed, and the powder feeding rate parameter had the lower effect. In laser cladding, when a molten pool is formed, there are several external and internal forces. External forces depend on nozzle design, powder flow settings, shielding gases, and transfer pressure. Internal forces of the molten pool are composed of buoyancy and Marangoni forces. Buoyancy forces are caused by the density difference in the molten pool. Marangoni forces in the absence of a surface active agent are dependent on the surface tension gradient induced by the temperature gradient in the molten pool [34]. In the absence of a surface active agent, the warmer liquid metal with lower surface tension at the center is pulled outward by the cooler

liquid metal with higher surface tension at the edge. In other words, an external shear stress on the pool surface is created by the surface tension gradient along the pool surface. This causes the liquid metal to flow from the center of the pool surface to the edge and return below the pool surface. As a result, the width of the track increases with the increase of laser power [35]. This issue is in agreement with the research results of Barekat et al. [33]. The clad layer with poor diffusion bonding with the substrate as a result of low dilution is the important and main characteristic of the laser cladding [12, 15]. Assuming that the clad track is a hemisphere, the geometrical dilution can be calculated from laser clad height (H) and the clad penetration depth (b) according to Eq. (1) [12]:

$$\text{Geometrical dilution} = \frac{b}{(H+b)} \quad (1)$$

According to results, the clad depth and dilution percentage are related to all parameters such as laser power, laser scanning speed, and powder feeding rate. According to the results of Fig. 4, the value of dilution changes from 3 to 74%. Increasing the laser power leads to an increase in the values of clad track penetration depth and dilution and has the most effect as compared with other parameters. In general, the laser power has an effect on the geometry of the molten pool and has a direct relationship with the cladding thickness, width, and depth of the molten pool [36,37]. According to the results of Fig. 4, at a constant powder feeding rate and laser scanning speed, higher laser power can increase the heat input, and more laser energy is absorbed by the substrate. Therefore, the substrate melts significantly, and as a result, the penetration depth and dilution increase. The wetting angle plays an important role in preventing porosity and appropriate overlapping. Also, reducing surface oxides for creating interfaces of clad metal is also necessary to achieve appropriate wetting [12, 33]. Assuming that the clad track is a hemisphere, the wetting angle can be calculated from the laser track width (W) and the laser clad height (H) according to Eq. (2) [15]:

$$\theta = 2\arctan\left(\frac{2H}{W}\right) \quad (2)$$

The values of the wetting angle of the single clad tracks of Stellite 6 were calculated with the image analysis software, according to Eq. (2). Based on the results of Fig. 4, the value of the wetting angle changes from 19.1 to 103°. According to the results, the wetting angle is related to all three parameters of laser power, laser scanning speed, and powder feeding rate. With increasing the power and scanning speed of the laser, the wetting angle decreased, and with increasing the powder feeding rate, the wetting angle increased.

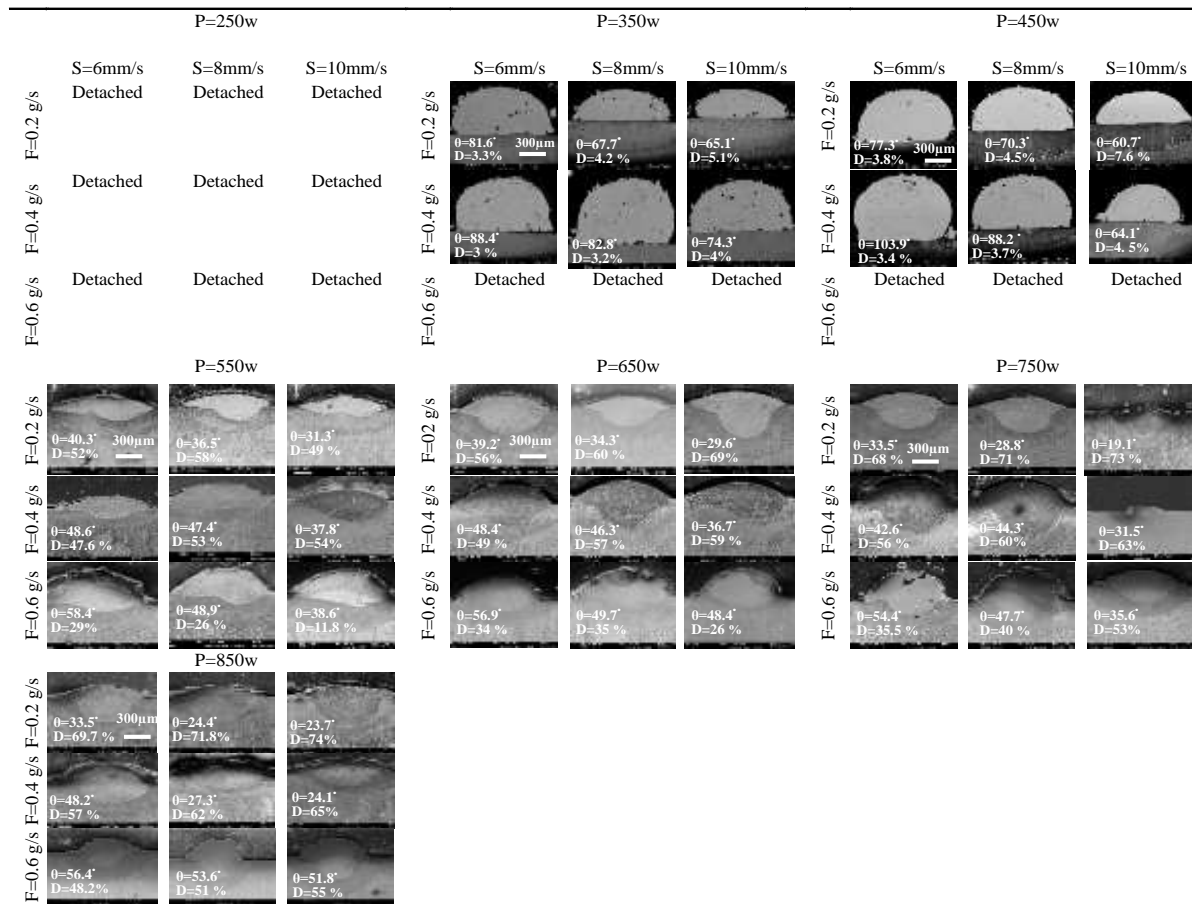


**Fig. 4.** Cross-sectional SEM micrographs of the single clad tracks of Stellite 6. For each laser power, laser scanning speed (S) increases from the left to the right and the powder feeding rate (F) increases from the top to the bottom.

Fig. 5 shows a cross-sectional SEM micrograph of the optimal single clad track of Stellite 6 with the values of clad height, clad track penetration depth in the substrate, wetting angle, and thickness. According to the review and comparison of the optimization process parameters of single clad tracks produced by

laser cladding with a laser power of 550 W, the laser scanning speed of 10 mm/s, and a powder feeding rate of 0.6 g/s, with a minimum dilution below 12% and an appropriate wetting angle, which caused the creation of a cladding with appropriate microhardness, was chosen as the optimal cladding.

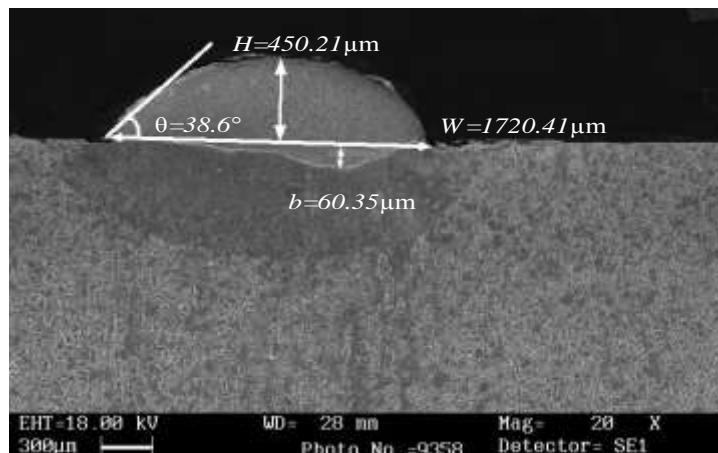


**Fig. 5.** Cross-sectional SEM micrograph of optimal single clad track of Stellite 6.

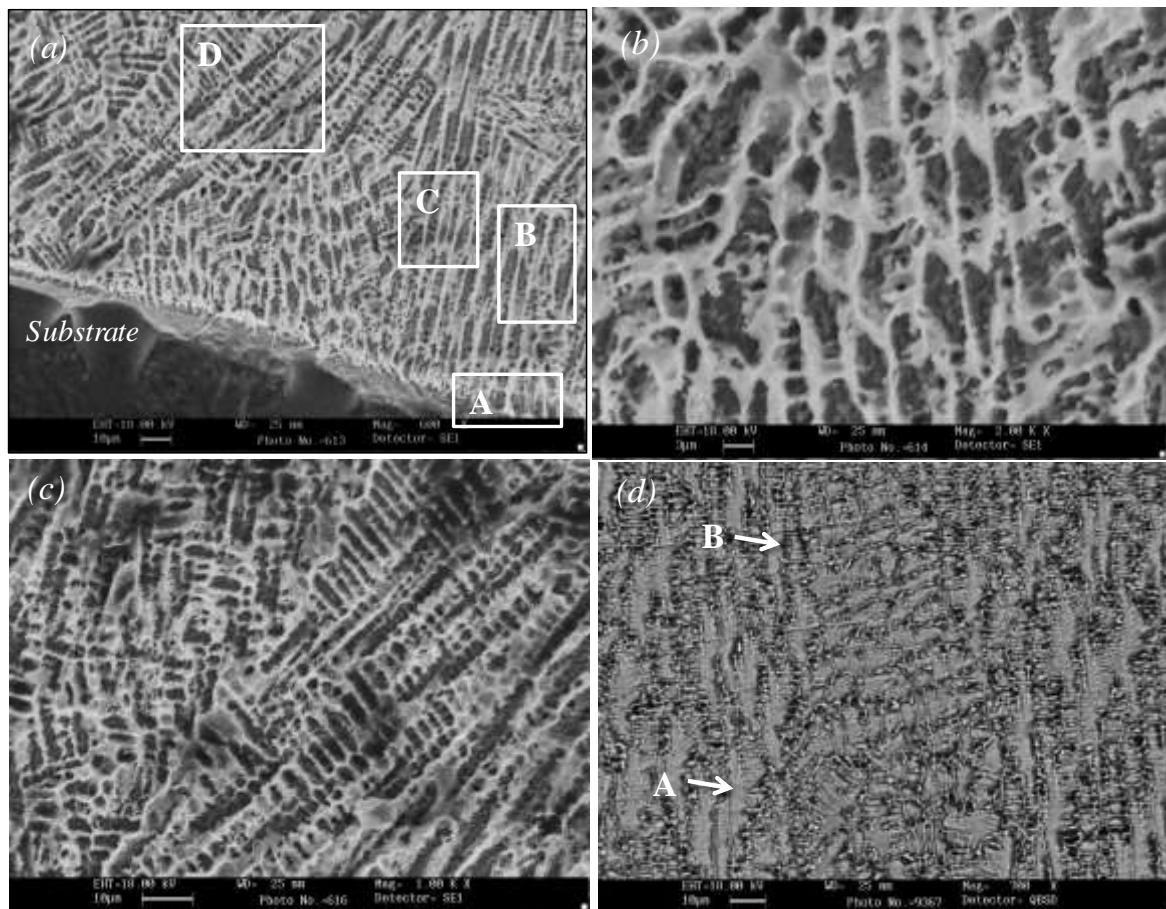
### 3.2. Microstructure of single clad track of Stellite 6

Fig. 6(a) shows a cross-sectional SEM micrograph of a single clad track of Stellite 6, which indicates a crack- and porosity-free structure with a thickness of

about 450 μm and good metallurgical bonding with the substrate. As can be seen, the solidification state and the size of the dendrites changed from the cladding/substrate interface towards the clad surface. The microstructure near the interface of the cladding

and the substrate is planar (areas A). Further, by moving away from the interface, the microstructure changed to coarse and fine columnar dendritic (areas B and C), and finally, the fine equiaxed dendritic microstructure (area D) was observed on the surface of the cladding. It can be recognized that the average size of dendrites also decreased from the interface towards the cladding surface. Fig. 6(b and c) shows the SEM micrographs of B, C, and D areas at higher magnification. The heat at the bottom of the molten pool is transferred from the substrate to the outside. The temperature gradient ( $G$ ) at the cladding/substrate interface is high enough. Therefore, at the interface, the  $G/R$  ratio is high, and the solidification speed ( $R$ ) tends to 0. As a result, the solidification is in planar mode. Approaching the surface of the molten pool, the temperature gradient ( $G$ ) decreases, and the solidification rate near the surface sharply increases, resulting in the transition from planar to dendritic solidification mode [38]. Fig. 6(d) shows the cross-sectional BSE SEM micrograph of Stellite 6 cladding at a distance of about  $442\ \mu\text{m}$  from the interface and near to the surface. The hypoeutectic microstructure, which includes primary dendrites (point A) and interdendritic eutectics (point B), was seen. The results of EDS analysis of these areas are presented in Table 4. According to the results, it was found that

the matrix dendritic phase (point A) is Co-rich and contains amounts of Fe and Cr, while the interdendritic phase (point B) is Cr-rich and contains amounts of Co. Since the C element is one of the light elements and the sensitivity of EDS is too poor to detect this element, therefore, the results are presented regardless of the C percentage, and only the C percentage in Table 4 is used for comparison. By comparing the chemical composition of the primary Stellite 6 powder in Table 2 with the EDS analysis of the Stellite 6 cladding in Table 4, it is concluded that there are not many changes in the chemical composition of the cladding. The content of the main component of Stellite 6, Co, in the cladding is only slightly less than the original amount. Also, a small amount of Fe has diffused from the substrate to the cladding, which shows that the process was carried out with appropriate parameters and caused the degree of dilution to be relatively controllable. Also, according to the EDS analysis presented in Table 4, the interdendritic phase of the stellite 6 cladding is Cr-rich and is higher than the initial chemical composition of the stellite 6 powder, which indicates the diffusion of Cr from the substrate to the cladding, which leads to the formation of carbides and, as a result, better resistance to wear and hardness of cladding [21].



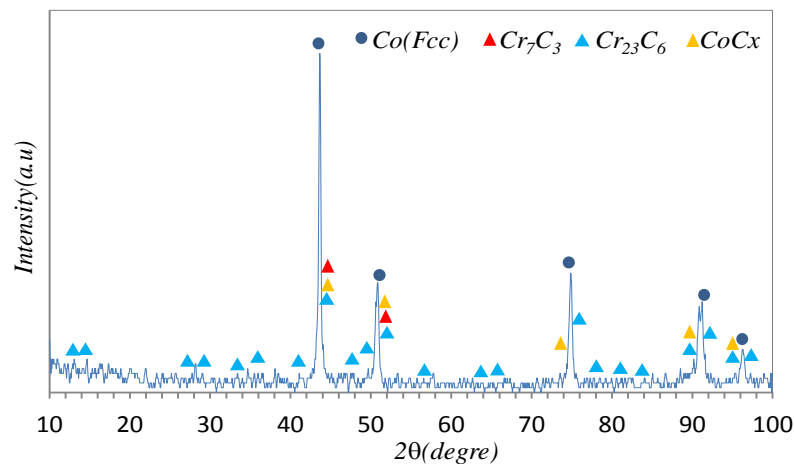
**Fig. 6.** SEM micrographs of (a) cross-sectional microstructure of single clad track of Stellite 6 and, (b) the image of areas B and C at higher magnification, (c) the image of area D at higher magnification and (d) BSE SEM micrograph of image (a) at a distance of  $442\ \mu\text{m}$  from the cladding surface.

**Table 4.** EDS Analysis of the different areas marked in Fig. 6(d)

Element (% wt.)	Series	Area	
		A	B
C	K	0.71	4.24
Al	K	0.06	0.09
Co	K	52.68	24.91
Cr	K	26.98	48.76
Mn	K	1.48	1.31
Mo	K	0.25	0.30
Fe	K	8.34	9.78
Ni	K	3.72	3.40
W	L	5.78	7.21

In order to investigate the possible phases in different microstructural regions observed in Fig. 6, the XRD analysis was done from the clad surface (Fig. 7). As seen, the main phase is  $\gamma$ -Co (fcc). Carbide phases such as  $\text{Cr}_{23}\text{C}_6$ ,  $\text{Cr}_7\text{C}_3$ , and  $\text{CoCx}$  are also observed. With the diffusion of C from the substrate to the cladding, the amount of C in the cladding increases, which leads to the formation of chromium carbides

and, as a result, increases the hardness and wear resistance [21]. By combining the results of EDS and XRD, it can be concluded that the microstructure of the Stellite 6 clad includes  $\gamma$ -Co (fcc)-rich solid solution eutectics containing a small amount of Fe and Cr, and also Cr-rich interdendritic eutectics consisting of  $\text{Cr}_{23}\text{C}_6$  and  $\text{Cr}_7\text{C}_3$  carbides.

**Fig. 7.** XRD pattern of Stellite 6 cladding.

In order to investigate the solidification of phases in the microstructure of Stellite 6 cladding, the equilibrium phase diagram (Co-C-%30Cr) was used. The dashed line in the Co-C-%30Cr phase diagram (Fig. 8) represents the used alloy (Stellite 6) in the current research. According to this figure, in the first stage of solidification for the alloy (near Stellite 6), by crossing the liquidus line, the  $\gamma$ -Co solid solution is first formed in cellular or dendritic form. According to this figure, in the initial stages of solidification for the alloy near Stellite 6, by cutting the liquidus line,  $\gamma$ -Co solid solution is first formed in cellular or dendritic form. At the same time, the interdendritic melt is enriched with C and Cr, and therefore the composition of the melt is near to the

eutectic composition. During the final stages of solidification, the formation of a eutectic solid solution from Co and Cr carbides occurs. Finally, it can be concluded that the microstructure of Stellite 6 cladding consists of  $\gamma$ -Co (fcc)-based solid solution, which is surrounded by eutectics consisting of  $\text{Cr}_{23}\text{C}_6$  and  $\text{Cr}_7\text{C}_3$  carbides [12,39]. According to Eq. (3), the G/R ratio decreases from the fusion line (FL) to the center line (CL). Therefore, the solidification mode changed from planar to cellular, columnar dendrite, and equiaxed dendrite throughout the melt zone [40].

$$\left(\frac{G}{R}\right)_{\text{CL}} \ll \left(\frac{G}{R}\right)_{\text{FL}} \quad (3)$$

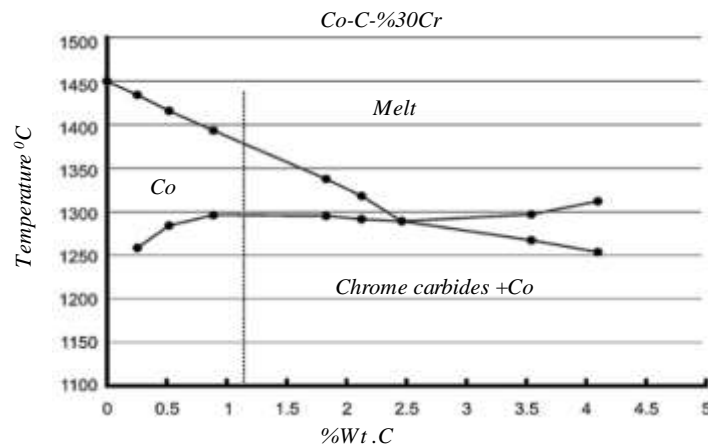


Fig. 8. Co-C-%30Cr equilibrium phase diagram [41].

### 3.3. Microhardness of Stellite 6 cladding

Fig. 9 shows the cross-sectional microhardness of a single clad track of Stellite 6. As can be seen, the microhardness increased by moving from the interface to the surface of the cladding, which can be attributed to the reduction in the size of the dendrites due to higher cooling rates and also the reduction of the dilution. During the process, the cladding/substrate interface is under the effect of the highest temperature; therefore, the cooling is slow during solidification, and the formed grains are coarse. In addition, in the vicinity of the interface, there is a higher dilution, which causes a greater

decrease in hardness owing to a decrease in the amount of C and Cr (decrease of hard carbide phases) in the cladding layer, which leads to a decrease in hardness. The average microhardness of the single clad track of Stellite 6 and the 35CrMo alloy steel substrate are 445 and 247, respectively. In general, the reason for the higher microhardness of the single-clad track of Stellite 6 is the presence of  $Cr_{23}C_6$  and  $Cr_7C_3$  carbides in the solid solution matrix of Co. Also, the W element in the Stellite 6 clad helps to increase the strength and microhardness. This issue is in agreement with the research results of Lin et al. [28] and Valsecchi et al. [26].

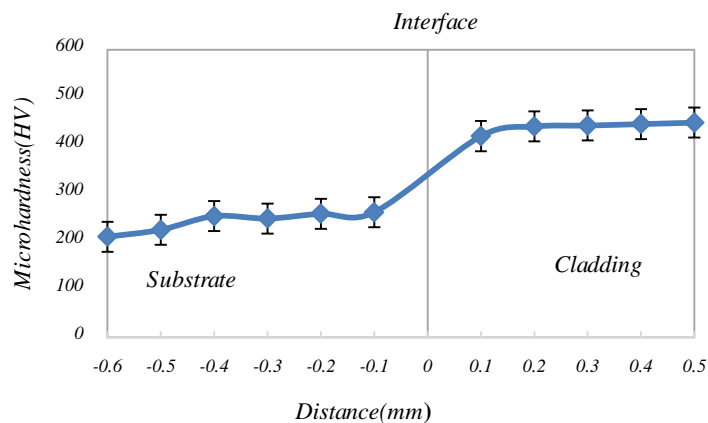


Fig. 9. Cross-sectional microhardness of single clad track Stellite 6.

### 3.4. Investigating the different ORs of single clad track of Stellite 6

In order to better understand the laser cladding process and the influence of the parameters, it is essential to produce a single clad track and investigate the geometry and mechanical properties of the cladding [15, 16, 42]. Assuming that the clad track is a hemisphere, the OR can be calculated from the laser track width (W) and the distance between neighboring tracks (D) according to the Eq. (4).

$$OR = \frac{(W-D)}{W} \quad (4)$$

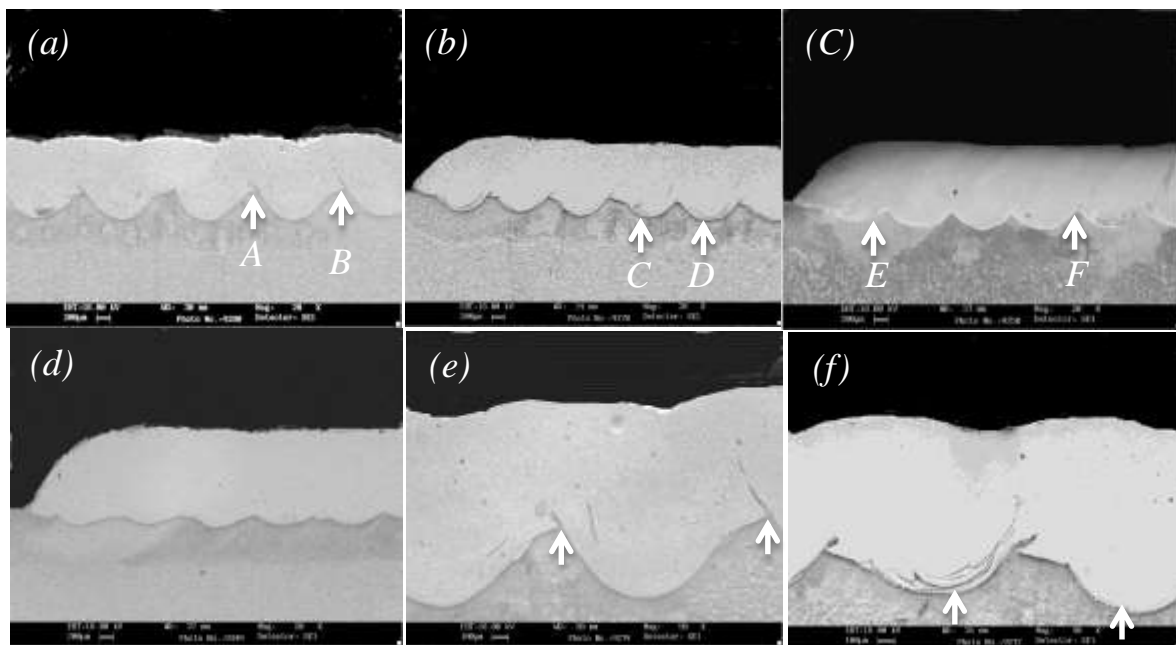
According to the optimal parameters of cladding presented before, ORs of 30, 40, 50, and 60% were used. Fig. 10 shows the cross-sectional SEM micrographs of the cladding layers with ORs of 30, 40, 50, and 60%. As can be seen in Fig. 10 (a, b, d, and e), in ORs of 30 and 40% in the interface of the passes, there are gaps, cracks, and pores, which cause a lack of complete bonding between successive passes. According to Fig. 10 (c) in OR of 50%, holes and cracks reduced. According to Fig. 10(d), in OR of 60%, a uniform and continuous cladding with minimum porosity was achieved. Dark spots in the

cladding can be the result of the gas confinement of the protective environment, atmosphere, and carrier gas during solidification, unmelted powder particles, and also impurities. The values of height, dilution, and depth penetration of cladding layers with different ORs are given in Table 5. According to the

presented information in Table 5 and also Fig. 10(d), it can be concluded that the Stellite 6 cladding with OR of 60% has a higher height, lower dilution, lower percentage of porosity, and more importantly, without cracks as compared with other ORs.

**Table 5.** Parameters of the cladding layer with different ORs

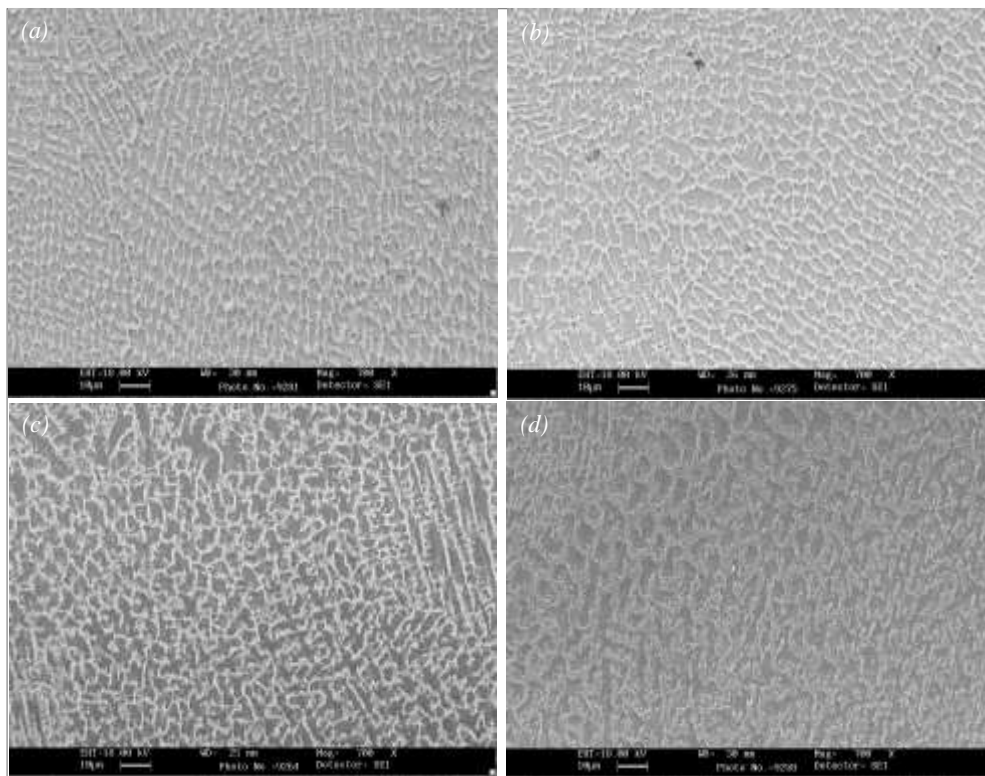
Overlapping rate (%)	cladding parameter		
	h( $\mu$ m)	b( $\mu$ m)	D(%)
30	665.27	310.30	31
40	871.17	214.12	20
50	983.54	140.56	12
60	1285.94	111.02	7



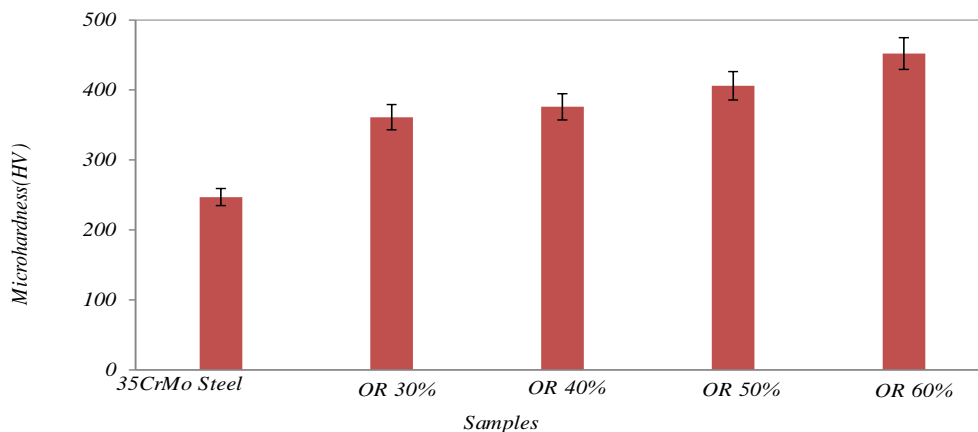
**Fig. 10.** Cross-sectional SEM micrographs of single track clad of Stellite 6 with different ORs of (a) 30%, (b) 40%, (c) 50%, and (d) 60%, (e) areas A and B from image (a) with higher magnification and (f) areas C and D from image (b) with higher magnification.

Fig. 11 shows the cross-sectional SEM micrographs of Stellite 6 cladding with different ORs. The average thickness of dendrites affects the microstructure, making it thinner and thereby increasing the strength [30,43,44]. Fig. 12 shows the cross-sectional microhardness of claddings with ORs of 30, 40, 50, and 60% as compared with the 35CrMo alloy steel substrate. As can be seen, in an OR of 30%, the microhardness changes of the cladding layer are more than the substrate. The microhardness increased

from 247 HV to 361 HV in OR of 30% and further to 376 HV in OR of 40%. By increasing the OR to 60%, the microhardness reached the highest value of 452 HV. The reason for the increase in the microhardness in OR of 60% compared to other ORs, according to Table 5, is more clad height and, as a result, lower dilution (lower diffusion of Fe from the substrate to the surface cladding) and also, according to Fig. 11(d), the finer equiaxed dendrite microstructure with minimum crack and porosity.



**Fig. 11.** Cross-sectional SEM micrographs of laser-cladded Stellite 6 with different ORs of (a) 30%, (b) 40%, (c) 50% and (d) 60%.



**Fig. 12.** The microhardness of laser-cladded Stellite 6 with different ORs as compared with the 35CrMo alloy steel substrate.

#### 4. Conclusions

In the present research, the characteristics of laser-cladded Stellite 6 on the surface of 35CrMo alloy steel were investigated. Also, optimizing the Stellite 6 cladding using different parameters of laser cladding, the effect of overlapping ratio, microstructure, and mechanical properties of the cladding were investigated, and the following results were obtained:

1. Laser power had a lower effect on the clad height. By increasing the powder feeding rate and reducing the laser scanning speed, interaction between powder and laser energy increased, and therefore, more amounts of powder reached molten temperature and led to more height of the clad track.

2. By increasing the laser power and decreasing the laser scanning speed, the clad track width increased. Also, the laser power effect was greater than the laser scanning speed, and the powder feeding rate parameter had the lower effect.

3. The clad track penetration depth was primarily proportional to the laser power, while the powder feeding rate and laser scanning speed had a lower influence on this parameter. 4. With increasing the power and scanning speed of the laser, the wetting angle decreased, and with increasing the powder feeding rate, the wetting angle increased. 5. The optimal parameters for the single-track laser-cladded Stellite 6 on the 35CrMo alloy steel substrate were found to be a laser power of 550 W, a laser scanning

speed of 10 mm/s, and a powder feeding rate of 0.6 g/s, resulting in an average dilution below 12%.

6. The microstructure of the laser-cladded Stellite 6 on the 35CrMo alloy steel substrate transitions from planar to columnar dendritic and finally to equiaxed dendritic as it moves from the interface to the cladding surface. This microstructure included  $\text{Cr}_{23}\text{C}_6$  and  $\text{Cr}_7\text{C}_3$  inter-dendritic eutectics within the  $\gamma$ -Co (fcc) matrix.

7. The microhardness of the Stellite 6 cladding was at about 452 HV, which was higher than the microhardness of the substrate. The hardness of the cladding changed with the distance from the interface due to the microstructural variations along the cross-section of the cladding.

8. The cross-sectional microstructure of Stellite 6 cladding with different ORs was equiaxed dendritic. Additionally, in the microstructure of samples with ORs of 30%, 40%, and 50%, the amount of porosity was higher with some cracks. However, in OR of 60%, the surface microhardness increased.

**Conflict of interest:** On behalf of all authors, the corresponding author states that there is no conflict of interest.

## References

[1] Wang W, Zheng XT, Yu JY, Lin W, Wang CG, Xu JM. Time dependent ratcheting of 35CrMo structural steel at elevated temperature considering stress rate. *Mater High Temp* 2017; 34: 172–178.

[2] Zhang JW, Lu LT, Shiozawa K, Zhou WN, Zhang WH. Effect of nitrocarburizing and post oxidation on fatigue behavior of 35CrMo alloy steel in very high cycle fatigue regime. *Int J Fatigue*. 2011;33(7):880–886.

[3] Yue W, Sun XJ, Wang CB, Fu ZQ, Liu YD, Liu JJ. A comparative study on the tribological behaviors of nitride and sulfur-nitrided 35CrMo steel lubricated in PAO base oil with MoDTC additive. *Tribol Int* 2011;44(12):2029–2034.

[4] Fernands FAP, Herk SC, Pereira RG, Picon CA, Nascente PAP, Casteletti. LC. Ion nitriding of a superaustenitic stainless steel: wear and corrosion characterization. *Surf Coat Technol* 2010; 204:3087–90.

[5] Cassar G, Avelar-Batista Wilson JC, Banfield S, Housden J, Matthews A, Leyland. A. A study of the reciprocating sliding wear performance of plasma surface treated titanium alloy. *Wear* 2010; 269:60–70.

[6] Tang WY, Chuang MH, Chen HY, Yeh JW. Microstructure and mechanical performance of new  $\text{Al}_{0.5}\text{CrFe}_{1.5}\text{MnNi}_{0.5}$  high entropy alloys improved by plasma nitriding. *Surf Coat Technol* 2010; 204:3118–3124.

[7] Wang HD, Zhuang DM, Wang KL, Liu JJ. Anti-scuffing properties of ion sulfide layers on three hard steels. *Wear* 2002; 253:1207–1213.

[8] Wang HD, Zhuang DM, Wang KL, Liu JJ. Comparison of the tribological properties of an ion sulfurized coating and a plasma sprayed FeS coating. *Mater Sci Eng* 2003; 357:321–327

[9] Xiao ZB, Huang YC, Liu Y. Plastic deformation behavior and processing maps of 35CrMo steel. *J Mater Eng Perform* 2016; 25:1219–1227

[10] Zhang J, Xue Q, Li S-X, Qin Z. Microstructure, corrosion and tribological properties of Ti(CN) multilayer coatings on 35CrMo steel by CVD. *Rare Met* 2014; 22:1314–1320.

[11] Jendrzejewski R, Conde A, De Damborenea J, Sliwinski G. Characterisation of the Laser-Clad Stellite Layers for Protective Coatings. *Mater Des* 2002;23:83–88.

[12] Toyserkani E, Khajepour A, Corbin S. Laser Cladding, CRC PRESS 2005

[13] Arias-Gonzalez F, del Val J, Comesana R, Penide J, Lusquinos F, Quintero F, Riveiro A, Boutinguiza M, Pou J. Laser cladding of phosphor bronze. *Surf Coat Technol* 2017; 313:248–254

[14] Lisiecki A, Iizak D, Kukofka A. Robotized Fiber Laser Cladding of Steel Substrate by Metal Matrix Composite Powder at Cryogenic Conditions, *Mater Perform Charact* 2019; 8: 1214–1225

[15] De Olivera U, Ocelik V, DE Hosson JThM. Analysis of coaxial laser cladding processing condition. *Surf Coat Technol* 2005; 197: 127–136

[16] Barnes S, Timms N, Bryden B, Pashby I. High power diode laser cladding. *J Mater Process Tech* 2003; 138: 411–416

[17] Ocelik V, Nenadl O, Palavra, DE Hosson JThM. On the geometry of coating layers formed by overlap. *Surf Coat Technol* 2014; 242 :54–61

[18] Nemecek S, Fiserova P. The Corrosion Resistance of Laser-Cladded Layers, Conf. *Laser Application in Industry* 2015; 16:18–3

[19] Xu GH, Kutsuna M. Characteristics of multilayer laser cladding using powder mixture of Co based alloy and Vanadium carbide. *Mater Sci Technol* 2008; 24:73–84

[20] Hou QY, Gao JS, Zhou F. Microstructure and wear characteristics of cobalt-based alloy deposited plasma transferred arc weld surfacing. *Surf Coat Technol* 2005, 194 (2–3) :238–243.

[21] Farnia A, Malek Ghaini F, Rao JC, Ocelik V, De Hosson ThM. Effect of Ta on the microstructure and hardness of Stellite 6 coating deposited by low power pulse laser treatments. *Surf Coat Technol* 2012; 213:278–284.

[22] Sh OC, Doh UM, Yoon IK, Lee DI, Kim JS. Effect of molybdenum on the microstructure and wear resistance of cobalt-base Stellite hardfacing alloys. *Surf Coat Technol* 2003;166: 117–126.

- [23] Tottel CR. An Encyclopdria of Metallurgy and Material British. Library catalog in publication elata 1984; 311
- [24] Sidhu TS, Prakash S, Agrawal RD. Studies of the metallurgical and mechanical properties of high velocity oxy- fuel sprayed stellite-6 coatings on Ni- and Fe-based superalloys. *Surf Coat Technol* 2006;201: 273-281.
- [25] Opris CD, Liu R, Yao MX, Wu XJ. Development of Stellite alloy composites with sintering/HIPing technique for wear-resistant applications. *MaterDesign* 2007; 28:581-591
- [26] Valsecchi B, Previtali B, Gariboldi E, Liu A. Characterisation of the Thermal Damage in a Martensitic Steel Substrate Consequent to Laser Cladding Process. *Phys Eng* 2011 ;10: 2851- 2856
- [27] Chang S, Wu H, Chen C. Impact Wear Resistance of Stellite 6 Hardfaced Valve Seats with Laser Cladding. *Mater Manuf Process*. 2008; 23:708-713
- [28] Lin C, Chen C. Characteristics of Thin Surface Layers of Cobalt-Based Alloys Deposited by Laser Cladding. *Surf Coat Technol* 2006;200: 4557-4563,
- [29] Sun S, Durandet Y, Brandt M. Parametric investigation of pulsed Nd: YAG laser cladding of stellite 6 on stainless steel. *Surf Coat Technol* 2005; 194:225– 231.
- [30] D Oliveira A, Silva P, Vilar R. Microstructural features of consecutive layers of Stellite6 deposited by laser cladding. *Surf Coat Technol* 2002; 153:203–209.
- [31] Xu G, Kutsuna M. Cladding with Stellite6/WC using a YAG laser robot system, *Surf Eng* 2006; 22:345-352
- [32] Toyserkani S, Khajepour E, Corbin A. Three-dimensional finite element modeling of laser cladding by powder injection: effects of powder feedrate and travel speed on the process, *J Laser Appl* 2003; 15:153–160.
- [33] Barekat M, ShojaRazavin R, Ghasemi A. Nd: YAG laser cladding of Co–Cr–Mo alloy on  $\gamma$ -TiAl substrate. *Opt Laser Technol* 2016; 80:145–152
- [34] Pinkerton A.J. University of Manchester, Laser direct metal deposition: theory and applications in manufacturing and maintenance, in: D.K.Y. Low, J. Lawrence, J. Pou, E. Toyserkani (Eds.), *Relat. Titles Adv. Laser Mater. Process. Technol. Res. Appl.*, Woodhead Publishing Limited, UK. 2010.
- [35] Ebrahimzadeh H, Mousavi SAAA. Investigation on pulsed Nd: YAG laser welding of 49Ni–Fe soft magnetic alloy. *Mater Des* 2012; 38:115–123.
- [36] Sudand W, Williams S. Investigation of the effects of basic laser material parameters in laser welding. *J Laser Appl* 2012; 24:032009.
- [37] Hofmeister W, Griffith M. Solidification in direct metal deposition by LENS Processing. *Met Mater Soc* 2001; 53:30–34.
- [38] Ding L, Hu S.S, Quan X.M, Shen J.Q. Effect of VN alloy addition on the microstructure and wear resistance of Co- based alloy coatings. *J Alloys Comp* 2016, 659,8–14.
- [39] Gholipour A, Shamanian M, Ashrafizadeh F. Microstructure and wear behavior of stellite 6 cladding on 17-4 PH stainless steel. *J Alloys Comp* 2011; 509:4905–4909.
- [40] Kou S. *Welding Metallurgy*. JohnWiley and Sons, New Jersey, 2003.
- [41] Fouilland L, Mansori M El, Massaqa A, Mater J. Friction-induced work hardening of cobalt- base hardfacing deposits for hot forging tools. *J Mater Proc Technol* 2009; 209: 3366–3373.
- [42] Chena B, Sua Y, Xieb Z, Tana C, Fenga J. Development and characterization of 316L/Inconel625 functionally graded material fabricated by laser direct metal deposition. *Opt Lasers Techno* 2020; 123:105916.
- [43] Naghiyan M, Shoja-Razavi R, Mansouri H, Jamali H. Microstructure investigation of Inconel 625 coating obtained by laser cladding and TIG cladding m. *Surf Coat Technol* 2018; 353:25-31.
- [44] Fenga K, Chena Y, Denga P, Lic Y, Zhaoc H, Lua F, Lid F, Huanga J, Lia Z, Improved hightemperature hardness and wear resistance of Inconel625 coatings fabricated by laser cladding. *J Mater Process Tech* 2017; 243: 82–91.